Correspondence to:

G. Hénaff,
gwendal.henaff@lpp.polytechnique.fr

A Compact Ion-Electron Plasma Camera Spectrometer With an Instantaneous Hemispheric Field of View

Gwendal Hénaff[1] , Matthieu Berthomier[1], Frédéric Leblanc[1], Jean-Denis Techer[1], Yvan Alata[1], and Carla Costa[2]

[1]Laboratoire de Physique des Plasmas (LPP), CNRS/UMR7648, Ecole polytechnique, Institut Polytechnique de Paris, Sorbonne Université, Université Paris-Saclay, Observatoire de Paris, Paris, France, [2]Centre National d'Etudes Spatiales, Toulouse, France

Abstract   Using additive manufacturing and a selective metalization technique, we have developed a compact ion/electron plasma camera based on the donut topology. With its instantaneous field of view of 2π sr, it eliminates the need for electrostatic deflectors. This 17 cm diameter plasma camera has an energy range from a few eV to 22 keV, an energy resolution of 10% and a geometric factor of 4.310^{-4} cm^2.sr.eV/eV per pixel, with 64 pixels corresponding to as many individual directions of observation. We have characterized its experimental response under an electron beam and compared it with numerical simulations. We have shown how carbon foils can be used as conversion layers to sequentially measure ions and electrons with a set of micro-channel plates biased at a fixed voltage. This principle was tested under electron and ion beams.

1. Introduction

Measurement of the distribution function of electrons and ions provides key information on the various plasma processes that shape the heliosphere, including magnetic reconnection, turbulent plasma transport, and particle energization at shocks, to name a few. The need to better monitor the fine structure of electron and ion velocity distribution functions (VDFs) in the solar wind and in planetary environments drove the design of the ever-improving plasma spectrometers that were used since the dawn of spaceflight (Neugebauer & Snyder, 1962). In 1982, a major milestone was achieved with the development of the top-hat electrostatic analyzer (ESA) (Carlson et al., 1982). Its electrostatic optics provides homogeneous sampling of phase space, typically within 5° of its viewing plane. The focusing properties of the top-hat ESA allow for high angular resolution in this plane, typically set at 5–20° depending on the capability of the detection system. Top-hat ESAs are defined by a limited number of geometrical parameters. Their optical properties are well described by simple analytical relationships between these parameters, enabling the instrument design to be rapidly adapted to a specific measurement requirement. For these many reasons, the top-hat ESA has become a reference instrument for space plasmas and planetary missions.

However, the near-planar field of view (FoV) of this plasma spectrometer does not allow the direct measurement of the complete 3D VDF of charged particles. On three-axis stabilized satellites, a classic approach to overcoming this limitation has been to combine the top-hat ESA with electrostatic deflectors (Burch et al., 2007; McComas, Zirnstein, et al., 2017; Sauvaud et al., 2008; Saito et al., 2010; Yokota et al., 2004) to sequentially scan out-of-plane viewing directions. At least two sensor heads are needed to cover the whole sky, with some important constraint on the measurement energy range, due to the high voltage required to deflect high-energy particles at large angles. Though very useful, this design strongly reduces the time resolution capability of plasma spectrometers since it couples the energy scan of the top-hat ESA with the angular scan of the deflection system. It also increases the complexity of the instrument's high voltage power supply (HVPS) which is used to bias both the energy analyzer and the electrostatic deflectors.

Several teams have aimed to design plasma instruments with an embedded instantaneous hemispheric FoV to overcome these limitations. The HYDRA instrument on NASA's Polar satellite (Scudder et al., 1995) used 12 individual cylindrical ESAs to cover one hemisphere with a coarse angular resolution and an energy range up to 35 keV/q. The DYMIO instrument on the Mars96 mission (Berthelier et al., 1998) had a 2π sr FoV with a 32° × 32° resolution but with a limited energy range up to 700 eV/q. More recently, The PICAM instrument on ESA's Bepi-Colombo mission was introduced by Vaisberg et al. (2016). PICAM has a 3D FoV but uses electrostatic mirrors, creating a strong constraint on the maximal energy range, which was set to 3 keV/q (Orsini et al., 2021).

On spinning satellites, top-hat ESA have been extensively used (Johnstone et al., 1997; McFadden et al., 2008; Rème et al., 1997), with the disadvantage of limiting the temporal resolution of plasma measurements to one or half a spin period, a few seconds in the best case. However, since the 1980s, the progress of space plasma science motivated the design of new space missions in order to unveil physical processes at kinetic scales. These scales, which are convected by fast plasma flows, translate into rapidly varying electron and ions VDF, that need to be monitored at sub-second time resolution. The NASA's MMS mission, which aimed to discover how magnetic reconnection works at electron scale in the Earth's magnetosphere, had to develop a new strategy to beat the spin period limit of plasma measurements. To achieve this task, the Fast Plasma Instrument (FPI) on MMS (Pollock et al., 2016) used 8 top-hat ESA to measure the electron VDF at 30 ms time scale and 8 other top-hat ESA to measure the ion VDF at 150 ms time scale. The 16 sensors also included a deflection system to scan out of plane viewing directions in 4 steps. The MMS approach made it possible to beat the spin period limit for the first time, but it involved a massive investment of the FPI team to build and inter-calibrate as many sensors on each of the 4 MMS spacecraft. FPI sensors mass reach 48 kg per satellite, or equivalently 3 kg per top-hat head with its deflection system and associated electronics. At a time when the next step in space plasma science is the deployment of even larger constellations (National Academies of Sciences, 2025; Retinò et al., 2022), it is difficult to imagine how such a strategy could be used without a spectacular increase in resources or without severely limiting a mission's ability to identify the kinetic processes that are ubiquitous and fundamental in space plasmas.

On the contrary, in recent years, the development of small satellites (Heidt et al., 2000) for both scientific and commercial applications has led the community to envisage new concepts for magnetospheric missions based on large constellations of small platforms (Retinò et al., 2022). However, achieving high temporal and spatial resolutions in this context is challenging, due to the limited resources available on small spacecraft. This has created a need for new instrument concepts that could go further than heritage systems (Zurbuchen & Gershman, 2016). The donut-shaped ESA concept (Hénaff & Berthomier, 2025; Morel et al., 2017) may provide an answer to this challenge, with a 3D FoV allowing instant coverage of a complete hemisphere, and with a high geometric factor (GF) per direction of observation to enable high temporal resolution measurements of the electron and ion VDF.

This paper shows the experimental performance of a specific implementation of the donut ESA that we have called 3DCAM. We first describe the numerical design and simulated performance of the electrostatic optics, and describe how a carbon foil can be used to operate the instrument for both ions and electrons with the same detector. We then present the additive manufacturing (AM) and functionalization process that has been developed to produce the electrostatic optics. The experimental performance of the donut analyzer is established with an electron beam and compared with numerical simulations. Then, using an ion beam, we show experimentally how thin carbon foils can be used to operate the instrument in electron or in ion detection mode. Finally, we summarize the results of this work and outline the development prospects for this new plasma spectrometer.

2. Instrument Design

As shown in Figure 1, the donut topology presents a rotational symmetry with 16 azimuthal sectors, each with 4 viewing directions in the polar dimension that converge to a disk-shaped detector plane. As a result, the donut analyzers can provide instantaneous imaging of the 3D flux distribution. In a previous work (Hénaff & Berthomier, 2025), we have shown that a wide range of these new ESAs topologies can be designed with various angular resolutions: low-resources donut electrostatic analyzers typically have a 22.5° × 22.5° angular resolutions with diameters below 20 cm. In contrast, high-resources designs will have a 11.25° × 11.25° with a wider diameter up to 30 cm.

The plasma camera instrument that we describe here is designed for constrained platforms, either small spacecraft dedicated to the monitoring of precipitating charged particles in the Earth's ionosphere, or larger satellites such as those developed for planetary missions, where individual instruments are limited in mass and volume. We aim to reach energies above 20 keV, to have an angular resolution of 22.5° × 22.5° covering the complete hemisphere with 64 viewing directions, and with a target diameter below 18 cm.

2.1. Geometric Parameters

In our previous work, we have shown that a reduced number of geometric parameters can be used to fully define the donut analyzer, provided that a few physical requirements are set. Table 1 summarizes the requirements used
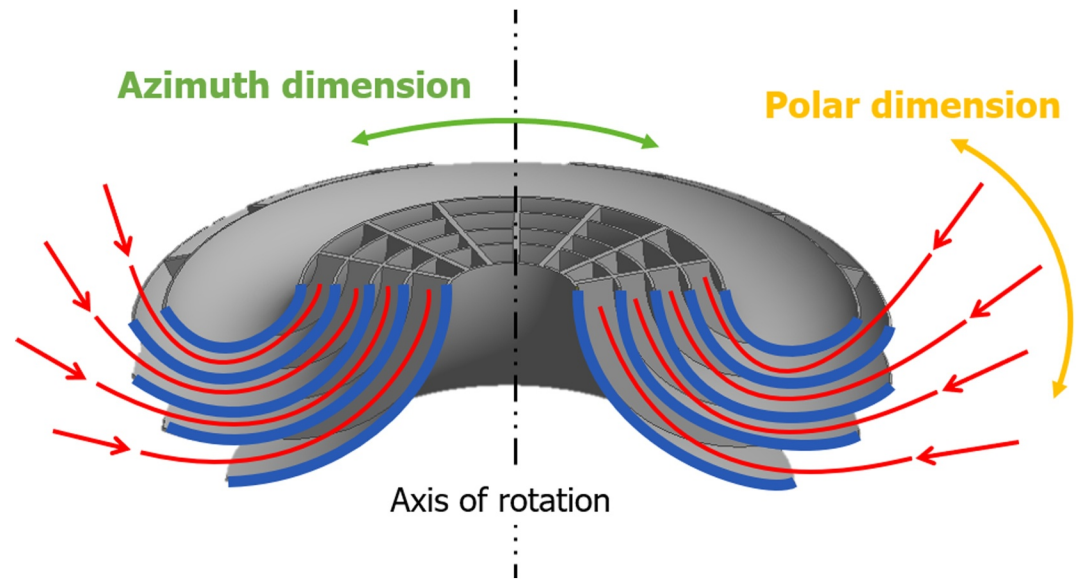
Figure 1. Cut view of a simplified donut analyzer topology: in red, electrons are entering the electrostatic optics from several polar directions. The instantaneous imaging of the polar and azimuthal dimensions gives the 2π sr field of view.

for designing the prototype, where EF_{max} is the highest acceptable electric field in the optics, E_{max} is the maximal detectable energy, and n is the number of polar channels, which sets the angular resolution of the instrument.

Once these requirements have been defined, and providing that we impose the same K-factor (i.e., the particle's energy per charge to electrode's voltage ratio) for all polar channels, the triplet of construction parameters $[R_d, d, D_1]$, fully define the geometry of the instrument (Hénaff & Berthomier, 2025).

R_d is the diameter of the micro-channel plates (MCP), D_1 is the interplate distance of the first polar channel, and d is the minimum stand-off distance between grounded and high-voltage biased electrodes: these parameters are shown on Figure 2, which shows a 2D cut view of the donut optics electrostatic potential map obtained with the SIMION-8 software (Dahl, 2000). The toroidal electrodes are biased at 150 V to select 1 keV electrons. Equipotentials are derived from the Laplace equations.

The triplet of parameters $[R_d = 36\ \text{mm},\ d = 1.1\ \text{mm},\ D_1 = 1.6\ \text{mm}]$ has been chosen for this model: the R_d parameter is compatible with standard size MCPs with an effective detection area of 77 mm (Hamamatsu, 2024). We aim for the highest sensitivity, which requires using the highest possible d value at a fixed R_d (Hénaff & Berthomier, 2025). This directly gives the remaining parameters as $d = 1.1\ \text{mm}$ and $D_1 = 1.6\ \text{mm}$.

Table 2 provides the interplate distances D_i and mean electrode radii R_i of the four polar channels. These parameters define a 64-channel donut analyzer with a total diameter of 17 cm, and a theoretical K-factor $K_{th} = 6.67$.

It should be noted that the electrodes consist of two conductive layers separated by a dielectric layer of thickness d. On Figure 2, this region appears open due to a limitation of Simion 8, which does not allow the implementation of non-conductive materials.

2.2. Numerical Simulations

The electrostatic behavior of the instrument can be fully characterized using numerical simulations. We used a particle pusher based on a Runge-Kutta fourth-order algorithm to fly particles with a variety of polar angles θ_i in 51 steps with a resolution of 0.5°, azimuth angles ϕ_j in 41 steps with a resolution of 1°, and energies E_k in 101 steps with an energy resolution of 0.3% through the donut optics. For each $[E_i, \theta_j, \phi_k]$ set, 512 particles are flown from random positions on the channel's entrance surface. This process is repeated for each polar channel, representing a total of 432 million particles. From these simulations, the polar acceptance $\Delta\Theta_{sim}$, the azimuth acceptance $\Delta\Phi_{sim}$,

Table 1
Physical Requirements of the Prototype

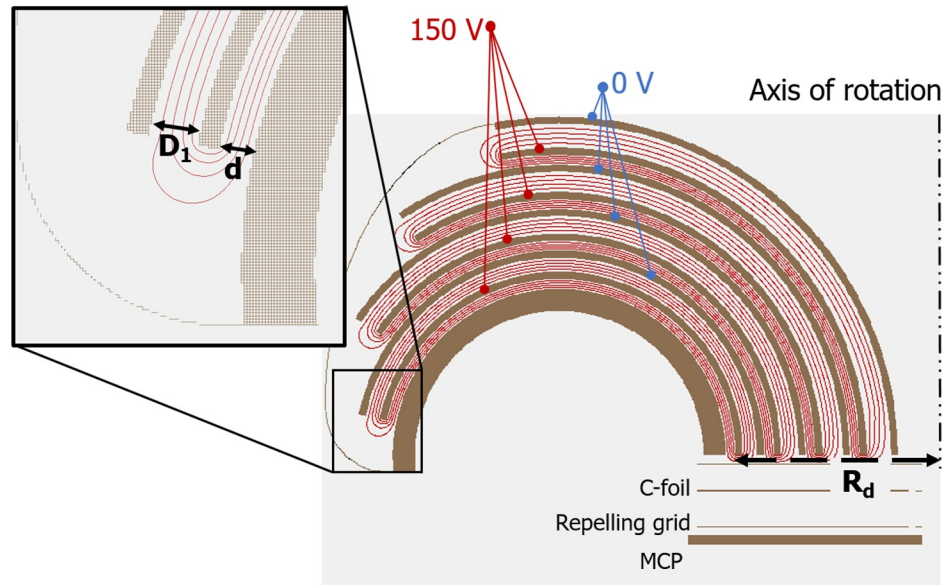| Angular resolution	n	Diameter (cm)	EF_{max}	E_{max}
22.5 ° × 22.5°	4	≤18 cm	3 kV/mm	22 keV

Figure 2. Cut view of the donut analyzer electrostatic potential map showing the four polar channels, and the location of various elements of the detection system.

and the energy acceptance $\Delta E/E_{\text{sim}}$ of the optics can be directly obtained and are presented in Table 3. These quantities are the full-widths at half-maximum of the integrated response in polar angles, azimuth angles, and energies of all particles reaching the detection system.

The GF is an important characteristics of electrostatic analyzers as it indicates the system's sensitivity. The effective time resolution capability of a plasma spectrometer is constrained by its GF. Its definition, however, varies among authors (Collinson et al., 2012). Here, we express the GF in cm^2 sr.eV/eV. It is given without attenuation factors: neither the Quantum efficiency Q_E of the MCP (Fraser, 1983), nor grid transparencies are included in our estimates. It is calculated as:

$$GF = \frac{1}{E_0{}^2} \int_{E_{\text{min}}}^{E_{\text{max}}} \int_{\theta_{\text{min}}}^{\theta_{\text{max}}} \int_{\phi_{\text{min}}}^{\phi_{\text{max}}} A\ R(E,\theta,\phi) \cdot E \cdot \cos^2\theta \cdot \cos\phi\ \ dE\ d\phi\ d\theta \qquad (1)$$

where E_0 is the peak of the energy response, A is the entrance area of the analyzer in cm^2, and $R(E,\theta,\phi)$ is the analyzer's response function at energy E and direction (θ,ϕ), indicating the fraction of incoming particles that reach the detector. The product $A\ R(E,\theta,\phi)$ gives the effective entrance surface of the instrument S_{eff} (Duvet, 2001; Morel et al., 2017). The calculated GF, S_{eff}, and K factor for each channel are reported in Table 3. The simulated K factor is derived from the averaged energy of the detected particles. Its channel to channel variation is of the order of ±1.5 %. We note some channel to channel variation of the other optics parameters, but the GF varies by less than 15% relative to its averaged value of 4.3 10^{-4}. We also note that a similar behavior is observed for top-hat ESA with deflectors where optics properties vary with the deflection angle (Pollock et al., 2016).

2.3. Ion-to-Electron Conversion Principle

When aiming to measure low-energy charged particles with an ESA and with a MCP-based detection system, one must post-accelerate these particles due to the MCP energy-dependent quantum efficiency Q_e. It has been shown by Fraser (1983, 2002) that electrons and ions need to reach a kinetic energy of respectively a few hundred eV and a few thousand eV to trigger secondary electron (SE) emission on the walls of the microchannels. Measuring both species with a single electrostatic head therefore requires switching the bias of the front plate of the MCP set from typically −500 V to +2,000 V. This approach was proposed for the AMBRE-2 laboratory prototype (Cara

Table 2

Inter-Plate Distance and Mean Radius of the Four Polar Channels of the Donut Electrostatic Analyzer Defined by the Triplet [36, 1.1, 1.6] *Making the Plasma Camera Instrument*

Channel	#1	#2	#3	#4
D_i (mm)	1.60	1.94	2.3	2.69
R_i (mm)	21.3	25.8	30.6	35.8

Table 3
Key Performance of the Donut Electrostatic Analyzer Defined by the Triplet [36, 1.1, 1.6] *Obtained Through Numerical Simulations*

	$\Delta\theta_{\mathrm{sim}}$	$\Delta\phi_{\mathrm{sim}}$	$\Delta E/E_{\mathrm{sim}}$	$GF_{\mathrm{exact,\ sim}}$ (cm^2.sr.eV/eV)	K_{sim}	S_{eff} (cm^2)
#1	5.0°	10.0°	9.0%	3.9 10^{-4}	6.3	0.30
#2	5.0°	14.0°	7.9%	4.1 10^{-4}	6.4	0.26
#3	5.5°	20.0°	8.8%	4.5 10^{-4}	6.5	0.21
#4	7.5°	22.0°	13.3%	4.9 10^{-4}	6.5	0.16
mean	5.7°	16.5°	9.7%	4.3 10^{-4}	6.4	

et al., 2017). But since it was expected that doing so would affect the electric properties of the MCP in the long term, such a design was not further developed.

Another technique to detect ions and electrons while keeping a fixed voltage bias on the MCP is to use carbon foils as an ion-to-electron conversion layer. This is a widely used solution on ion-mass spectrometers: in time-of-flight (ToF) systems (Saito et al., 2021; Rème et al., 2001; D. McComas et al., 2008), ions are accelerated to typically 15 kV to a Carbon foil (C-foil) and cross it with limited scattering due to their high kinetic energy, ending on a detector and generating a ToF stop signal. When crossing the C-foil, they may also emit a SE that is accelerated to another detector and generates a ToF start signal.

We use a similar principle to measure ions and electrons sequentially: in ion-measurement mode, a negatively biased C-foil can accelerate incident ions that are "converted" into SE. In electron-measurement mode, electrons are accelerated and pass through the positively biased C-foil almost unaffected while maintaining a fixed positive bias on the front plate of the MCP set in both cases. This principle has been implemented in flight by Yokota et al. (2024) on the SS250-3 rocket launch.

We expect that the C-foil should be first biased to a few hundred volts to sufficiently accelerate the electrons so that they cross the foil, and then to a few thousand volts (negative) to accelerate ions in such a say that they would emit SE. Unlike the use of C-foils in ion-mass spectrometers, foil-induced ion scattering is not the main concern of the design, as only SE are of interest in ion mode, and the MCP would be located in close proximity of the C-foil in order to avoid any significant cross-talk between adjacent pixels of the anode located under the MCP. This principle is illustrated in Figure 3 for low-energy electrons (left) and ions (right), with examples of voltage on the grids and MCP.

3. Prototype Design

3.1. Optics Manufacturing

The donut ESA cannot easily be manufactured using conventional machining techniques: it would require the assembly of dozens of individual elements, generating errors in interplate distance control, which would ultimately degrade the quality of the electrostatic environment and the optics performance. Recent advances in AM and polymer functionalization (Perera et al., 2023) have made it possible to obtain thick, high-quality metallic coatings deposited on 3D-printed plastics. In particular, several teams have used PLD-SLA (pulsed laser deposition stereo-lithography) to produce complex prototypes of millimeter-wave space antennas (de Rijk et al., 2013; von Bieren et al., 2014; Dimitriadis et al., 2016; Li et al., 2018; Teniente et al., 2018). In the case of plasma instruments, fuse-deposition AM was used to produce a prototype of a top-hat analyzer with an energy range of 10 eV–30 keV by Larrick et al. (2024). These advances paved the way for the production of the first functional prototype of a donut ESA using AM and chemical coating techniques.

Given the small interplate distance of this electrostatic optics, we opted for SLA manufacturing, which enables us to produce high-resolution objects. A SLA resin with high mechanical and thermal performance and low out-gassing properties was selected. The topology is printed with a vertical and horizontal resolution of 50 μm, allowing strict control of interplate distances. After careful inspection of all internal and external surfaces, we clean the 3 days-printed polymer in sonic baths, 10 min with acetone, and twice 10 min with ethanol. The optics is then chemically etched with an acid solution and activated with a colloid palladium bath. We use a commercial plating bath
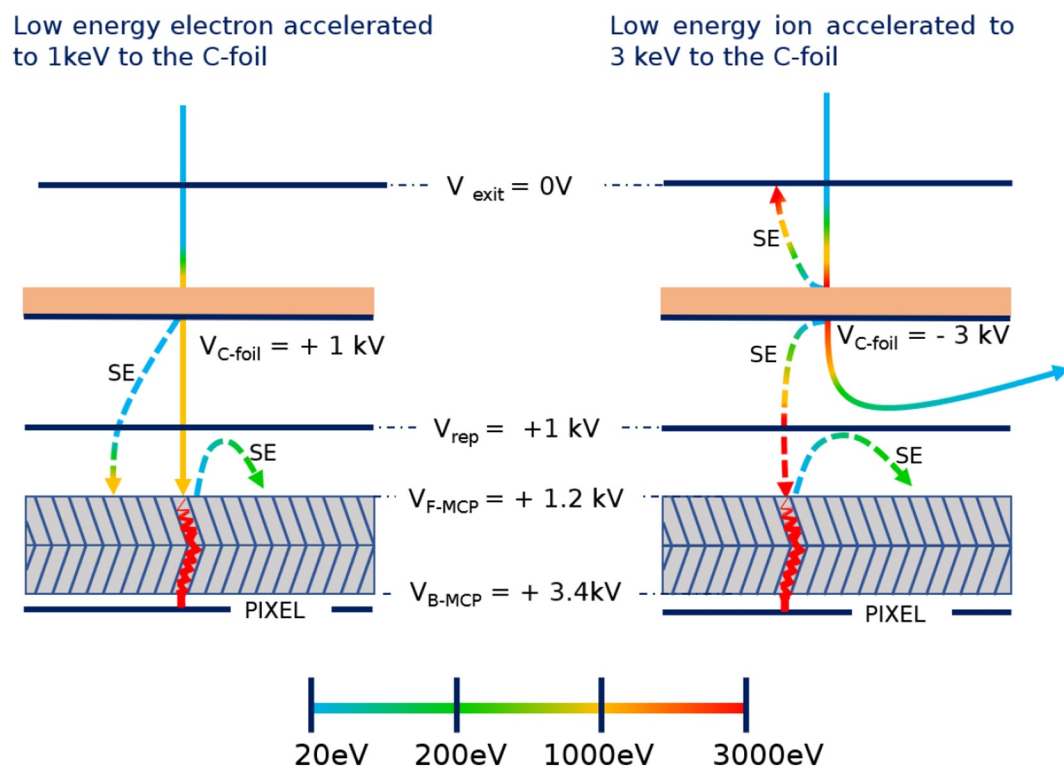
Low energy electron accelerated to 1keV to the C-foil

Low energy ion accelerated to 3 keV to the C-foil

$V_{exit} = 0V$

$V_{C\text{-foil}} = + 1\ kV$

$V_{C\text{-foil}} = - 3\ kV$

SE

SE

$V_{rep} = +1\ kV$

$V_{F\text{-MCP}} = + 1.2\ kV$

$V_{B\text{-MCP}} = + 3.4kV$

PIXEL

PIXEL

20eV 200eV 1000eV 3000eV

Figure 3. Use of a Carbon foil that allows the detection of low energy ions and electrons sequentially, with a fixed micro-channel plates voltage bias.

from MacDermid to deposit a 10 µm layer of chemical copper on the optics. We use proprietary techniques to avoid depositing copper in specific areas, as well as texturing, allowing to independently bias the two surfaces of the same electrode. Figure 4 shows the optics selectively plated with electroless copper.
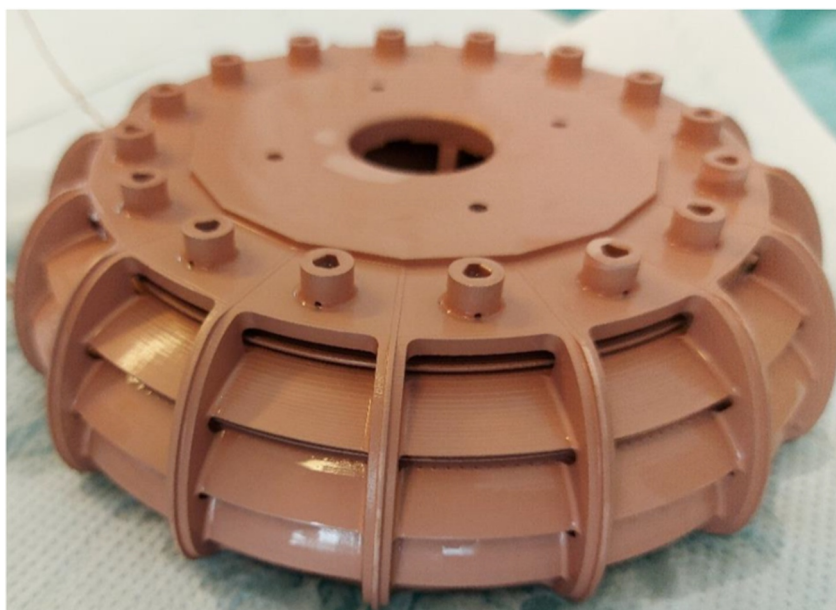
Figure 4. Donut optics after electroless copper coating.
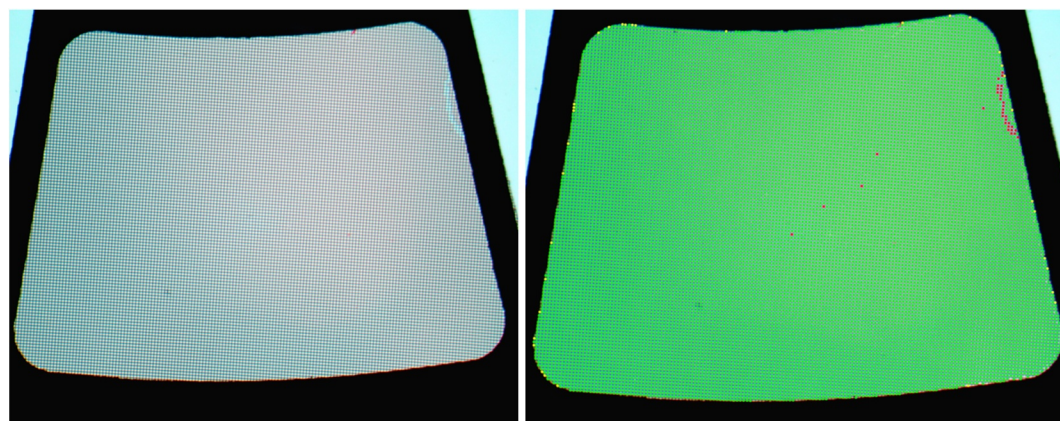
Figure 5. C-foil reaching integrity above 99.5%. Left: picture of the grid and foil. Right: in fake colors, intact cells (green) and broken cells (red).

A known difficulty when designing plasma instruments is to implement mitigation solutions for solar UV radiation, which otherwise reaches the MCP and generates charge clouds, saturating the detector and making it impossible to discriminate between the charged particle signal and the UV signal. Typical solutions revolve around the deposition of high-absorbance coatings on internal surfaces: a widely used process is the commercial Ebonol-C bath used for example, on SWAP/New-Horizons (D. McComas et al., 2008), CAPS/Cassini (Young et al., 2004) and JADE/Juno (McComas, Alexander, et al., 2017). The Ebonol-C bath is applied to copper and copper alloys: it grows a copper oxide with a dendritic shape that effectively limits the reflectance to a few percent, making it an ideal solution for absorbing UV radiation. Since our manufacturing process enables a layer of electroless copper to be deposited in excess of 20 μm, Ebonol-C is particularly suitable: only the top 2−3μm would be sacrificed to grow the black copper layer, as shown by Hooks et al. (2024). Due to the complex shape of these optics, applying Ebonol-C on the internal surfaces require the use of a proprietary masking technique that we have developed in-house.

3.2. C-Foil Manufacturing

We have deposited C-foils from The Arizona Carbon Foil Co., Inc. With a surface density of 0.5 μg/cm^2 on nickel grids with a mesh size of 333 lpi (line-per-inch), following the recommendations presented by D. J. McComas et al. (2004). We have developed an automated device for depositing C-foils on large grids with a surface of around 2 cm^2, while keeping a high integrity typically above 99%: Figure 5 shows a picture of one of these grids with the defective cells in fake colors.

3.3. Instrument Overview

The block diagram in Figure 6 shows, on the left, the three printed circuit boards developed for this instrument prototype. The Imaging Detection System (IDS) contains the C-foils, repeller grids, a set of MCP in chevron configuration, and an anode board shown on the bottom right. The anode board features 64 pixels on one side and, on the other side, four 16-channel ASICs that have been developed for the Solar Wind Analyzer of the ESA/NASA Solar Orbiter mission (Owen et al., 2020). The rad-hard ASIC includes 16 charge sensitive amplifiers and discriminators from noise. Detection thresholds are set by individual 10-bits Digital to Analog Converters that are configured through a Serial Parallel Interface. Individual logic pulses are routed toward the control board.

The FPGA (control) board manages these pulses by incrementing 16-bits counters. It controls the High-Voltage Power Supply (HVPS) board which provides the MCP bias and the polarization of the C-foils using high-voltage amplifiers. The HVPS board also includes the circuitry needed for the high-voltage sweep of the electrostatic optics bias, typically varying from −3.3 kV to −1.6 V in ion mode, and from 1.6 V to 3.3 kV in electron mode to cover the 10 eV to 22 keV energy range in 64 energy steps. The three printed circuit boards are stacked on top of the donut optics, as shown in Figure 6. In this configuration, the instrument has a diameter of 17 cm and a height of 12 cm, for a total mass of 1.8 kg.
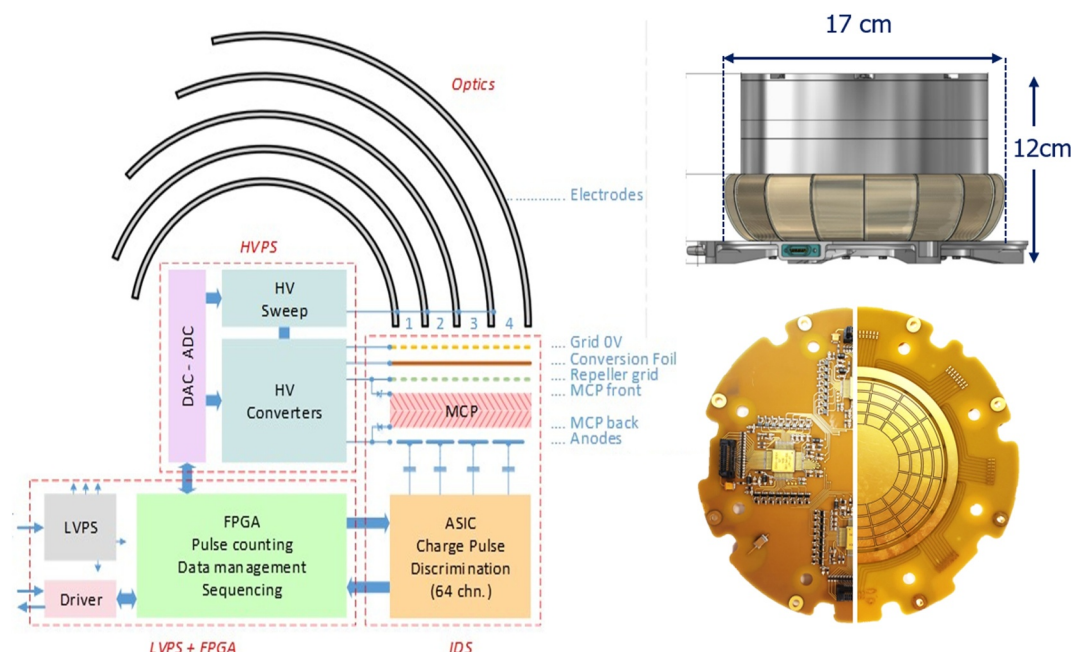
Figure 6. Left: block diagram of the instrument prototype; top right: side view of the CAD version of the instrument; bottom right: front and back of the detection board showing the 64 pixels anode and the four 16-channel charged particle discriminators ASIC.

4. Electrostatic Performances of the Donut Analyzer

4.1. Experimental Set-Up

The first series of beam tests we conducted were aimed at establishing the performance of the donut optics. In order to distinguish the intrinsic properties of the donut analyzer from the potential effects of the IDS, we used a simplified detection system with a 16-pixel anode, covering four azimuth sectors (labeled A to D) and four polar channels (numbered 1 to 4), as shown in Figure 7. The collected charge on these pixels was coupled to an Ortec 9327 amplifier located outside our vacuum chamber, for signal amplification and discrimination from noise: the 16 coaxial cables are visible in Figure 8. This electronics is coupled to external counters. The donut optics is electrostatically closed by 16 entrance grids, one per azimuthal sector. In Sector D, the high-transparency exit grid includes a thin C-foil, while sectors A to C have an exit grid without a C-foil.
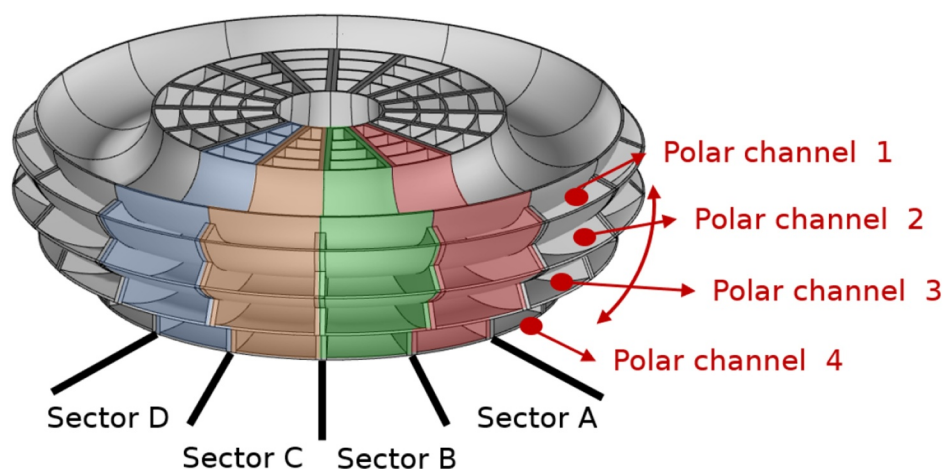

Figure 7. Numbering of azimuth sectors and polar channels tested with an electron beam.
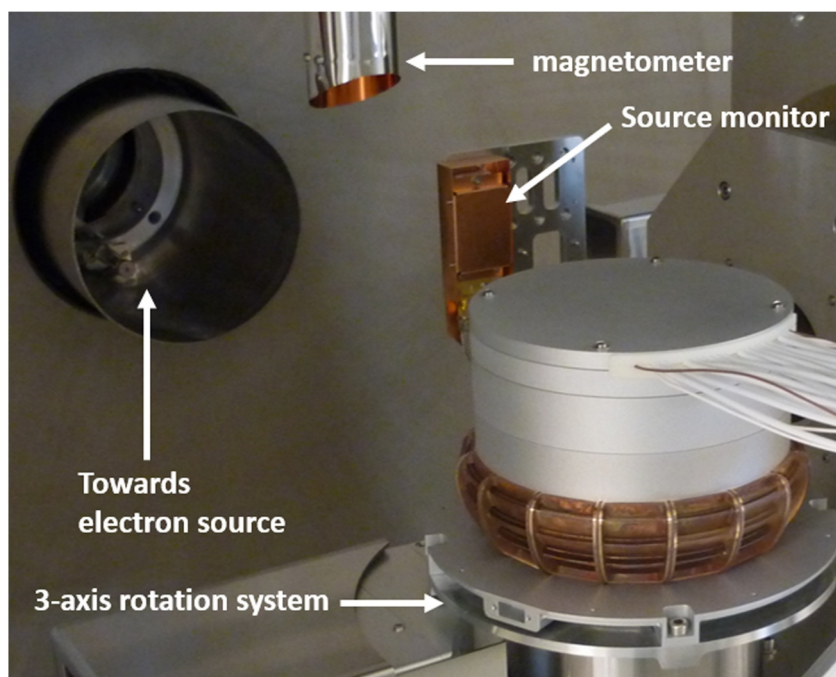
Figure 8. Electron beam test set-up in the LPP vacuum chamber.

We mounted the donut optics on a three-axis rotation system placed in front of our electron source, which operates according to the principle of photoelectric emission. A mercury-xenon arc lamp emits UV radiation at 253.6 nm, triggering the emission of low-energy photoelectrons from a gold photocathode biased at high-voltage. These electrons are accelerated by a grounded grid, producing a highly directional electron beam whose energy is adjustable and can vary between 10 eV and 30 keV. The 8 cm diameter electron beam is wide relative to the entrance surface of the optics.

The electron beam can be observed independently of the instrument using a dedicated source monitor shown in Figure 8. The magnetic environment is controlled using a fluxgate magnetometer, and the Earth's magnetic field is compensated for using a three-axis Helmholtz coil system surrounding the vacuum chamber. The rotation system allows the instrument to move in the polar and azimuthal directions relative to the electron beam. The third axis of rotation allows switching from one azimuthal sector to another.

4.2. Energy-Angle Response

The aim of this experiment is to quantify the energy-angle response of each of the polar channels of the optics, on different azimuthal sectors. The electron source is set to emit electrons at 4,000 eV.

By moving the instrument with the rotation system shown on Figure 8, the direction of the beam is changed from $-8°$ to $+8°$ in $0.5°$ steps around the normal to the aperture in the polar dimension. For each polar increment, the bias of the optics is changed from 528 to 693 V in 5 V steps. This measurement is carried for the four polar channels [1–4] on sectors [A–D]: This gives the 2D response illustrated in Figure 9 for Sector C. Because the numerical simulations are carried out by changing the energy of the beam while the experiments are carried out by changing the optics bias, the energy response is expressed in the dimension of K with $K = \frac{qE}{V_{\text{optics}}}$ in order to compare both the simulations and experiments. The next sub-sections are aiming to show the experimental variance from sector to sector and to compare these results with those of the numerical simulations.

Testing electrostatic analyzers on their full energy range is critical in order to ensure that remaining leaking fields do not impact the trajectory of deflected low energy particles, and that a high voltage bias can be successfully maintained without electric discharges. The donut analyzer have been successfully operated at a 30 V bias under a 200 eV beam, and at a 1.5 kV bias under a 10 keV beam. Preliminary tests have been carried out on representative geometries up to a 3.5 kV bias.
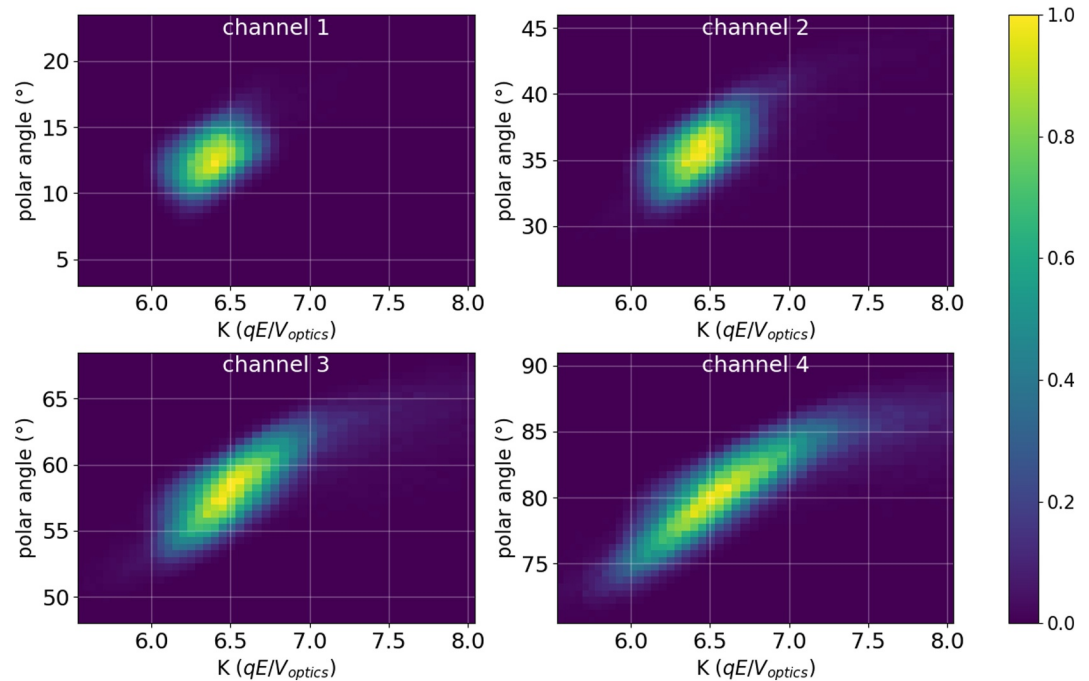
Figure 9. Experimental energy-angle response of sector C for each polar channels. The color-scale is showing the normalized number of counts.

4.2.1. Integrated Energy Response

Figure 10 shows each channel's integrated energy response on all polar angles. The response for each sector is shown in color, and the integrated simulated energy response is shown in black. Table 4 compares the differences between the simulated and experimental K-factors and the differences between the simulated and experimental energy acceptances ($\Delta E/E$).

A maximal difference between K_{sim} and $\overline{K_{\mathrm{exp}}}$ of 0.4 for channel 4 is observed. The energies acceptances vary at most of 2 points in the case of channel 1, indicating a good fit with the simulation. For channels 3 and 4, we observe a high-energy tail not present in the simulation. Channels 3 and 4 have a shorter arc length than channels 1 and 2 and a less-focused beam at the exit, therefore with proportionally more electrons interacting with the metal coating close to the exit. At high energies, they emit secondary electrons that cross the exit grid and are accelerated to the detector, increasing the number of counts and resulting in this tail effect.

4.2.2. Integrated Polar Response

In Figure 11, we show the experimental and simulated integrated polar response. In table 5, we compare the difference in the pointing direction between the simulation ($\Theta_{0,\,\mathrm{sim}}$) and the experiments ($\overline{\Theta_{0,\,\mathrm{exp}}}$). The pointing offset is below $1°$ in all cases, and the polar acceptance varies at most of $1.2°$ between $\Delta\Theta_{\mathrm{sim}}$ and $\overline{\Delta\Theta_{\mathrm{exp}}}$, giving high confidence in the simulation tools.

4.3. Azimuth Response

We experimentally measured the azimuth response on the four channels of Sector A at the peak of the energies and polar response, with $1°$ steps. We compare them to the simulated integrated azimuth response on Figure 12.

The experimental and simulated integrated azimuth response are quantified in Table 6: A systematic offset in the pointing direction is observed, ranging from $2°$ to $3°$. This discrepancy can be attributed to a $2°$ alignment error on one of the vacuum-grade rotations, which was identified after this measurement. As a result, the azimuthal response is truncated toward the negative angles by a few degrees, which is particularly noticeable in the response of channels 3 and 4.
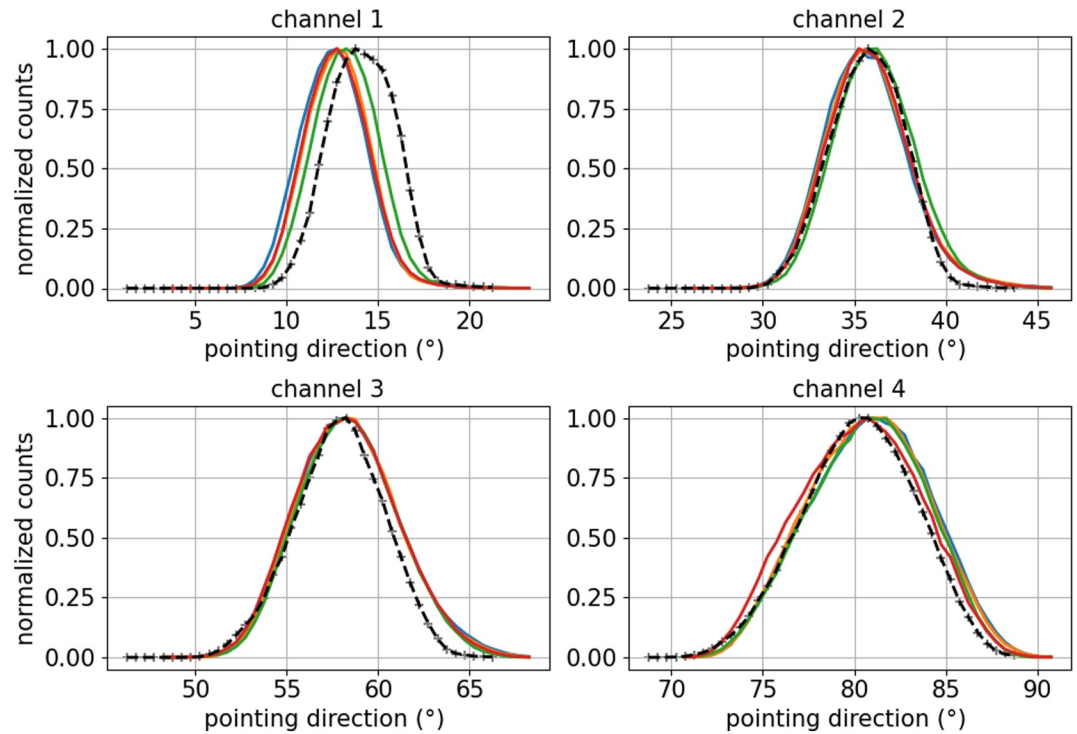
Figure 10. Integrated energy response for different channels. Blue: Sector D response, Orange: Sector C response, Green: Sector B response, Red: Sector A response. Black: simulated integrated energy response, with fitting.

4.4. Experimental Geometric Factor

An absolute characterization of the experimental GF, following Equation 1, would typically require an exact measurement of the beam current at the instrument's entrance and a precise characterization of its angular dispersion. It would also require a fine 3D scan across all polar angles, azimuthal angles, and energies for each polar channel and sector, resulting in a test duration of over 90 hr. Over such an extended period, the filament would reach half of its lifetime, causing the electron flux to decrease during the test, making this incompatible with the constraints of our test facilities.

Instead of performing the exact calculation of the GF shown in Equation 1, a simplified estimation of the experimental and simulated geometric factors can be made using Equations 2 and 3, allowing a direct comparison between the two.

$$GF_{\text{approx, sim}} = \Delta\Theta_{\text{sim}} \cdot \Delta\Phi_{\text{sim}} \cdot \Delta E/E_{\text{sim}} \cdot S_{\text{eff}} \tag{2}$$

$$GF_{\text{approx, exp}} = \Delta\Theta_{\text{exp}} \cdot \Delta\Phi_{\text{exp}} \cdot \Delta E/E_{\text{exp}} \cdot S_{\text{eff}} \tag{3}$$

Based on Equations 2 and 3, an approximate simulated GF can be calculated from the simulation data and compared to an approximate experimental GF derived from the measured acceptances presented in Tables 4–6. In both calculations, we use the simulated effective entrance surface, since the test setup does not allow for an exact measurement of the experimental effective entrance surface.

Table 7 compares the values of $GF_{\text{exact, sim}}$, $GF_{\text{approx, sim}}$ and $GF_{\text{approx, exp}}$ for each of the four polar channels of the donut analyzer. The exact simulated GF ($GF_{\text{exact, sim}}$) accounts for inter-dependencies between the polar angle Θ, azimuthal angle Φ, and energy $\Delta E/E$, resulting in a more consistent and reliable value. In contrast, the approximated GF ($GF_{\text{approx, sim}}$) only

Table 4
Experimental and Simulated Energy Response and K Factors for Each Channel

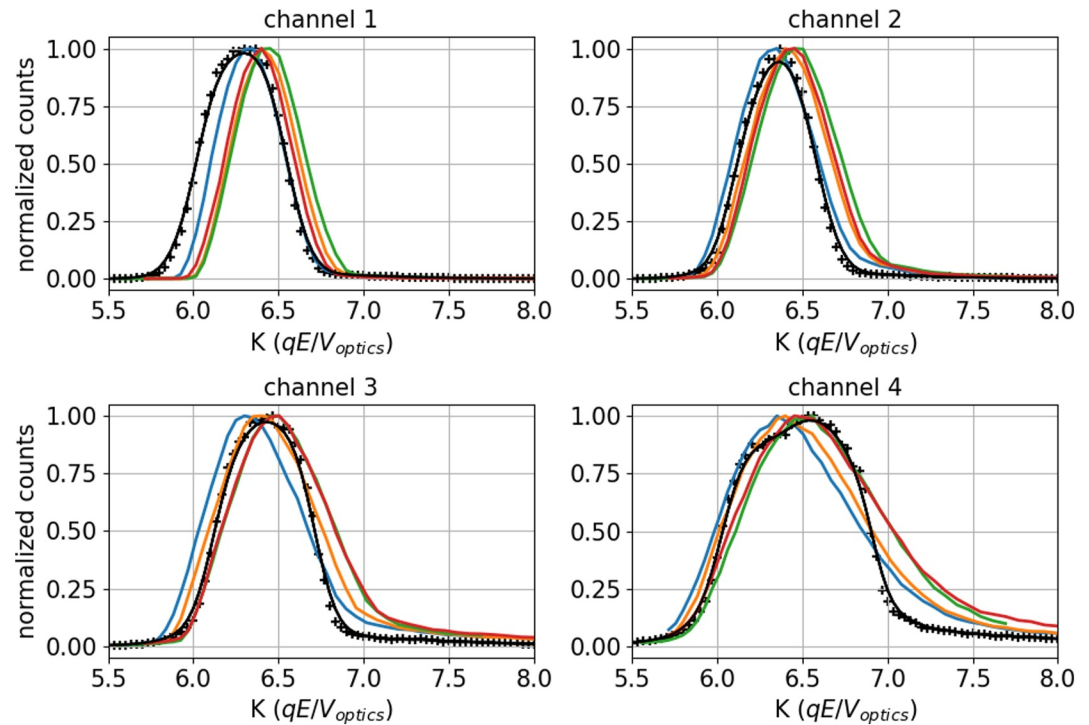|	K_{sim}	$\overline{K_{\text{exp}}}$	$(\Delta E/E)_{\text{sim}}$	$\overline{(\Delta E/E)_{\text{exp}}}$
Channel 1	6.30	6.41 ± 0.04	9.0%	7.0% ± 0.2
Channel 2	6.37	6.41 ± 0.05	7.9%	8.4% ± 0.2
Channel 3	6.47	6.42 ± 0.10	8.8%	10.5% ± 0.1
Channel 4	6.53	6.44 ± 0.09	13.3%	13.9% ± 0.4

Figure 11. Integrated polar response. Blue: Sector D response, Orange: Sector C response, Green: Sector B response, Red: Sector A response. Dotted-black: simulated integrated polar response, with fitting.

considers the FWHM of the response and does not account for these correlations, leading to higher values. The approximated experimental GF ($GF_{approx, exp}$) follows the same approximation, but its values exhibit greater variability due to measurement uncertainties and assumptions about the effective entrance surface. An exact measurement of the GF, accounting for a fine sweep on all energies and angles, and an experimental measurement of the effective entrance surface would increase the confidence in this result. Due to the setup's current limitations, this couldn't be carried out in this study. The purpose of comparing the approximated experimental and simulated geometric factors is to demonstrate that, under the same approximations, the two results differ only slightly, thus providing confidence in the reliability of the simulations.

5. A C-Foil as an Ion/Electron Conversion Layer

One of the challenges of these performance tests is to experimentally verify the behavior of carbon foils. Previous studies (Allegrini et al., 2003; Ritzau & Baragiola, 1998) have shown that the surface density of carbon foils can vary from the manufacturer's stated density by a factor of 3–4. The effective thickness of the carbon foil directly influences the specifications of the high-voltage power supplies used to post-accelerate particles before they encounter the foil, and determines the spacing between the foil and the repeller to prevent electrical breakdown.

The upcoming tests have two main objectives. First, we aim to determine the acceleration voltage required for a low-energy electron beam to pass through the carbon foil successfully. Second, we aim to establish the necessary acceleration for low-energy ions to generate at least one forward SE capable of reaching the detection system.

5.1. C-Foil Under an Electron Beam

We set the instrument to face Sector D, where a C-foil is mounted above the detector. The electron source emits and accelerates low-energy electrons to 200 eV toward the C-foil, and the front of the MCP is set at 400 V. We increase the C-foil bias from 0 to 1.3 kV.

Table 5
Experimental and Simulated Polar Response and K Factors for Each Channel

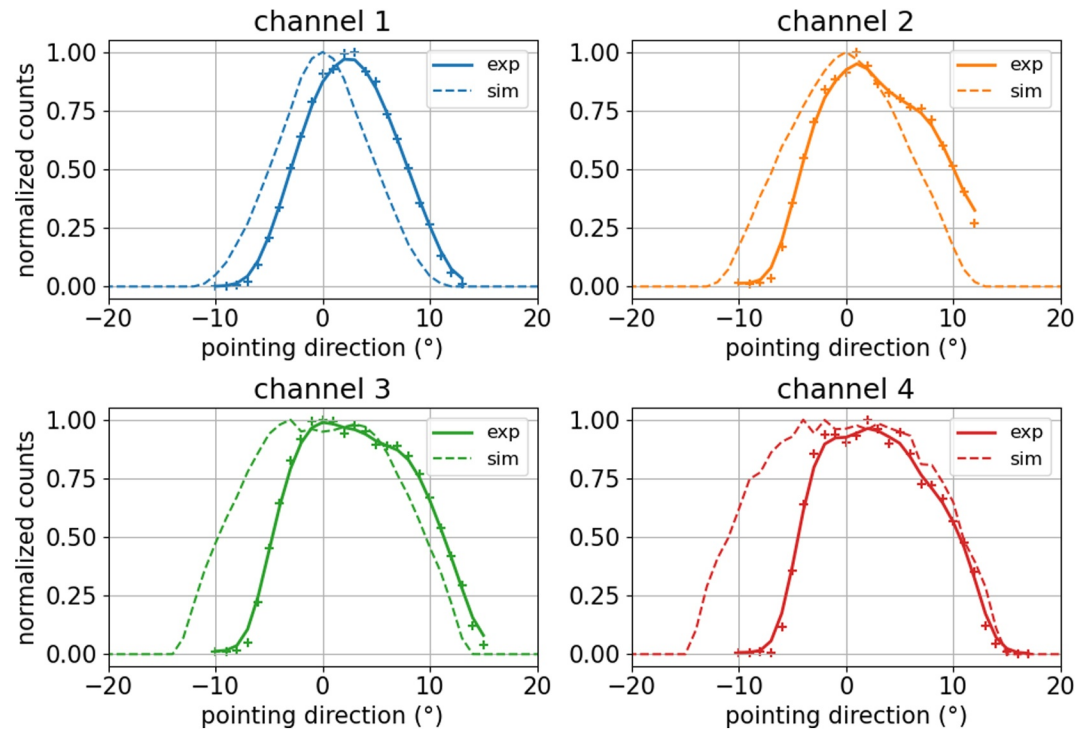|	$\Theta_{0, sim}$	$\overline{\Theta_{0, exp}}$	$\Delta\Theta_{sim}$	$\overline{\Delta\Theta_{exp}}$
Channel 1	13.75°	12.9 ± 0.18°	5.0°	4.1 ± 0.24°
Channel 2	35.75°	35.6 ± 0.28°	5.0°	5.4 ± 0.24°
Channel 3	58.25°	58.2 ± 0.14°	5.5°	6.9 ± 0.24°
Channel 4	80.25°	81.0 ± 0.19°	7.5°	8.6 ± 0.31°

Figure 12. Experimental response of the polar channels of Sector C, compared to the simulated integrated azimuth response, with fitting.

Figure 13 shows the evolution of the number of counts on the detector while we increase the bias of the C-foil. At low energies, the incident electrons don't have enough energy to cross the C-foil and are absorbed, resulting in a low count number. With the increase of their kinetic energy, statistically more electrons cross the C-foil and increase the number of counts on the MCP. When the incident electrons have enough energy, the number of counts stabilizes and a plateau effect is observed, as all electrons pass through the C-foil. This indicates the voltage needed to accelerate the low-energy electrons so that 90% crosses the carbon foil: from Figure 13, this value is found at 1.2 kV (accounting for the initial 200 eV kinetic energy of the ions), therefore validating the principle of transparency of the C-foil under accelerated electrons.

5.2. C-Foil Under an Ion Beam

With the rotation system, we move the instrument by 90° to face a Colutron G-2 ion source shown in Figure 14 and coupled to a Wien Filter, allowing to select the ions depending on their charge-on-mass ratio: we use it to generate a He^+ ion beam at 500 eV.

The instrument is positioned so channel 3 of Sector D faces the beam. The repeller grid voltage is set to 1.2 kV, while the front of the MCP is maintained at 1.3 kV. We slowly change the C-foil bias from +300 V to −2.4 kV, increasing the kinetic energy of the incident ions at the C-foil from 200 eV to 2.9 keV. After passing through the foil, the ions encounter an electric field at 1.2 kV + k_E(ions)/q that effectively repels them away from the MCP while accelerating the forward SE toward the detector, as shown in Figure 3. This setup prevents double detection, which could otherwise occur due to the delay in the arrival of the forward SEs and the transmitted ions at the MCP.

In Figure 15 (left), we show the evolution of the number of counts on the MCP when the kinetic energy of the He^+ ions at the C-foil increases. We observe a behavior similar to the electron measurements in Figure 13. At low energies (200 eV), the ions don't have enough energy to cross the C-foil and don't emit forward SEs: the number of counts is close to 0. When their kinetic energy

Table 6
Experimental and Simulated Azimuth Response and K Factors for Each Channel

	$\Phi_{0,\,sim}$	$\Phi_{0,\,exp}$	$\Delta\Phi_{sim}$	$\Delta\Phi_{exp}$
Channel 1	0°	2 ± 0.3°	10°	11 ± 0.4°
Channel 2	0°	2 ± 0.3°	14°	14 ± 0.4°
Channel 3	0°	3 ± 0.3°	20°	16 ± 0.4°
Channel 4	0°	3 ± 0.3°	22°	16 ± 0.4°

Table 7
Exact and Approximated Experimental Geometric Factors

	$GF_{\text{exact, sim}}$ $\left(\text{cm}^2.\text{sr}.\frac{\text{eV}}{\text{eV}}\right)$	$GF_{\text{approx, sim}}$ $\left(\text{cm}^2.\text{sr}.\frac{\text{eV}}{\text{eV}}\right)$	$GF_{\text{approx, exp}}$ $\left(\text{cm}^2.\text{sr}.\frac{\text{eV}}{\text{eV}}\right)$
#1	$3.9 \ 10^{-4}$	$4.1 \ 10^{-4}$	$(2.9 \pm 0.2) \ 10^{-4}$
#2	$4.1 \ 10^{-4}$	$4.4 \ 10^{-4}$	$(5.0 \pm 0.3) \ 10^{-4}$
#3	$4.5 \ 10^{-4}$	$6.2 \ 10^{-4}$	$(7.4 \pm 0.3) \ 10^{-4}$
#4	$4.9 \ 10^{-4}$	$10.1 \ 10^{-4}$	$(9.3 \pm 0.5) \ 10^{-4}$
mean	$4.3 \ 10^{-4}$	$6.2 \ 10^{-4}$	$(6.1 \pm 0.2) \ 10^{-4}$

increase, the probability of reaching the end of the foil and emitting a forward SE increases. The ions eventually reach an energy threshold at which most incident ions emit a forward SE, and a plateau is observed.

We compare this experimental behavior to simulations performed using the SRIM/TRIM software (Ziegler et al., 2010): several ion-in-matter simulation runs were carried out with 10^4 He$^+$ ions flown. On each run, the energy of the incident ions is increased, and the ratio between transmitted ions and emitted ions is measured. This is done for several carbon foils of different surface densities: 1.5 µg.cm^2 and 2 µg.cm^2.

The experimental behavior fits with the simulation carried out for foils with a 2 µg.cm^2 surface density, 4 times the theoretical thickness of the foil: this is consistent with the literature on foils from this manufacturer (Ritzau & Baragiola, 1998). It also gives the voltage bias that allows the C-foil to operate as a conversion layer for incident Helium ions. As shown in Figures 15, a 2 kV bias allows 90% of these ions to cross the foils, effectively demonstrating the principle of using carbon foils as ion-to-electron conversion layers.
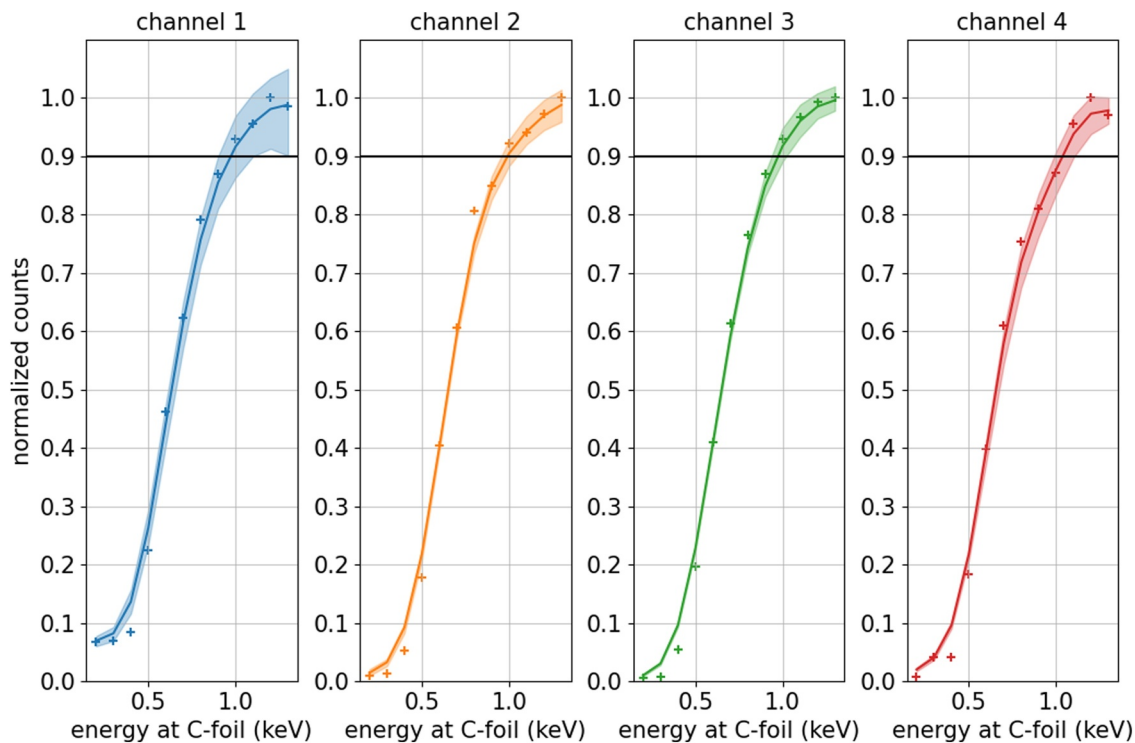

Figure 13. Evolution of the number of counts as a function of the energy of the electrons at the C-foil on different polar channels. Experiments are carried three times per channel. The mean value is showed by the markers, the variance is shown by the shaded areas.
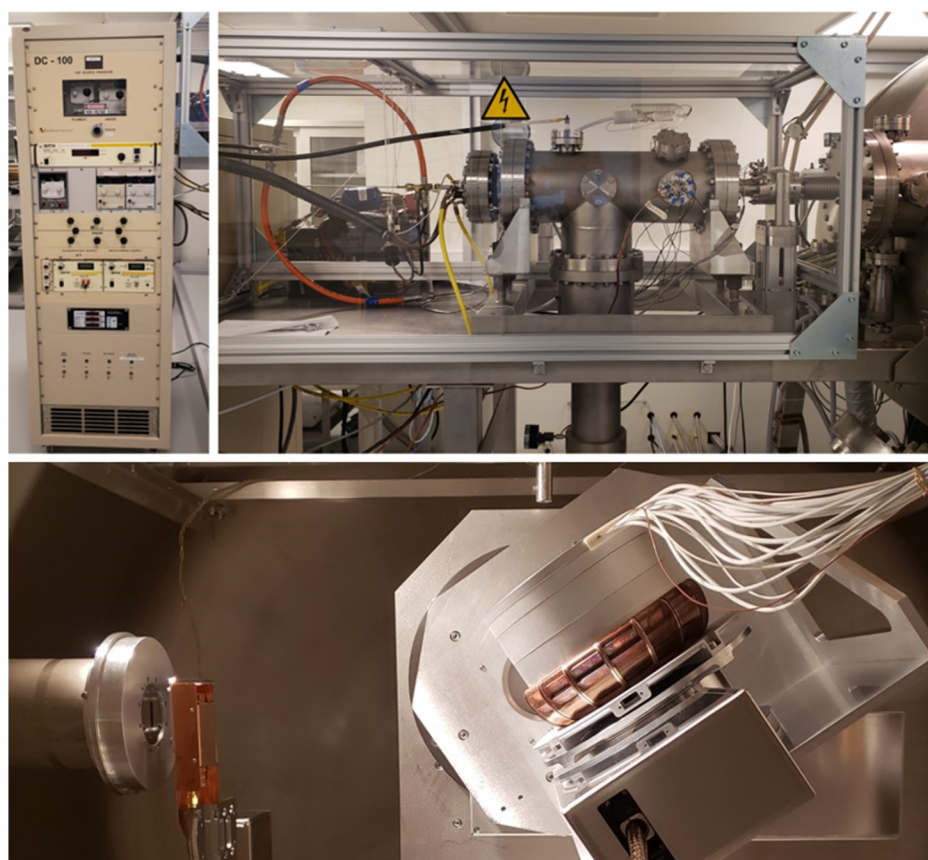
Figure 14. Top: ion source setup. Bottom: instrument facing the ion source.

6. Conclusion

We proved that the donut analyzer can be manufactured using AM and selective electroless plating, which is, to our knowledge, a first in plasma instrumentation development. These new techniques allow us to approach these new topologies without requiring complex machining and assembly, therefore potentially reducing the production cost. We established the electrostatic behavior of the donut analyzer under electron beams, characterized its polar, azimuth, and energy response, and compared it to numerical simulations. We found a clear fit between the experimental and numerical results, indicating the accuracy of these simulations and giving confidence in the results of the broad parametric study we have published (Hénaff & Berthomier, 2025). We showed how a carbon foil can be used as an ion-to-electron conversion layer, allowing to measure the 3D distribution function of both species with a single electrostatic head and a single set of MCPs at a fixed bias.

Thanks to CNES's demonstration program, we are now developing the Qualification Model of the 3DCAM instrument, the next iteration of the instrument described in this paper with improved performance. This instrument will include dedicated radiation hardened FPGA and HVPS boards and will undergo mechanical, thermal and environmental testing by the end of 2026. We are also targeting an in-orbit demonstration in 2028. This instrument is expected to be a 1.75 kg sensor, the donut optics is 17 cm wide, the total height is 12 cm, with a 2π sr FoV and a $22.5° \times 22.5°$ angular resolution. It has 64 viewing directions, a larger energy range from 10 eV to 25 keV and an increased effective GF per pixel of $4 \ 10^{-4}$ cm^2 sr.eV/eV.

Overall, this research has demonstrated the feasibility of using the donut topology concept for in situ characterization of space plasmas. The main advantage of this design is its instantaneous hemispheric FoV: compared to an instrument with the same GF that needs n deflections to cover the complete hemisphere, plasma cameras can operate n times faster with the same count rate.
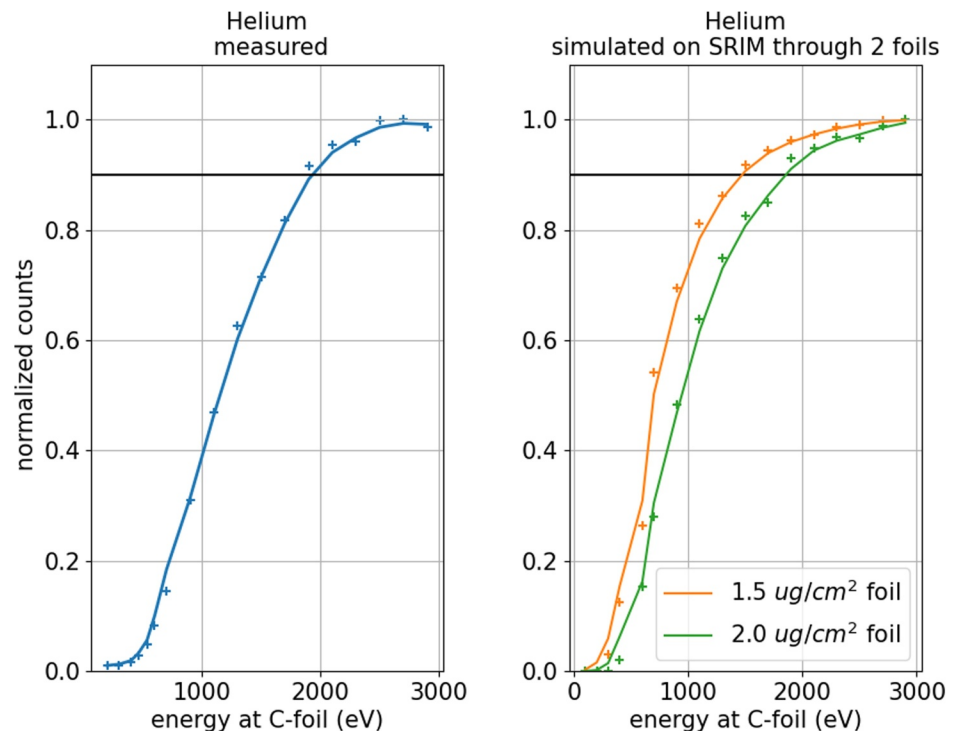
Figure 15. Left: experimental measurement of the number of electron counts on the micro-channel plates depending of the energy of the ions, with fitting. Right: simulation of the evolution of transmitted ions in a C-foil depending on their energy with fitting, for two types of C-foil with different surface densities.

The plasma camera's demonstrated performances open the way to new mission concepts based on constellations of several small spacecraft dedicated to the study of the earth magnetosphere: it has the main advantage of sampling through the complete hemisphere while having a resolution independent of the spin period of the spacecraft, for a mass equivalent to a single top-hat instrument. On planetary missions where platforms are three-axis stabilized, coupling this new analyzer to a dedicated time-of-flight system could bring new capabilities to the in-planning planetary exploration programs, such as the NASA Uranus Orbiter and Probe mission and the European Space Agency L4 toward Enceladus.

Conflict of Interest

The authors declare no conflicts of interest relevant to this study.

Data Availability Statement

The calibration's raw data files are available in their original .csv format at https://zenodo.org/records/15056829 (Hénaff, 2025).

References

Allegrini, F., Wimmer-Schweingruber, R. F., Wurz, P., & Bochsler, P. (2003). Determination of low-energy ion-induced electron yields from thin carbon foils. *Nuclear Instruments and Methods in Physics Research Section B: Beam Interactions with Materials and Atoms*, *211*(4), 487–494. https://doi.org/10.1016/S0168-583X(03)01705-1

Berthelier, J.-J., Illiano, J. M., Hodges, R. R., Covinhes, J., Godefroy, M., Gogly, G., et al. (1998). The dymio ion mass spectrometer of the Mars 96 mission. In *Measurement techniques in space plasmas: Particles* (pp. 215–220). American Geophysical Union (AGU). https://doi.org/10.1029/GM102p0215

Burch, J. L., Goldstein, R., Cravens, T. E., Gibson, W. C., Lundin, R. N., Pollock, C. J., et al. (2007). RPC-IES: The ion and electron sensor of the rosetta plasma consortium. *Space Science Reviews*, *128*(1), 697–712. https://doi.org/10.1007/s11214-006-9002-4

Cara, A., Lavraud, B., Fedorov, A., De Keyser, J., DeMarco, R., Marcucci, M. F., et al. (2017). Electrostatic analyzer design for solar wind proton measurements with high temporal, energy, and angular resolutions. *Journal of Geophysical Research: Space Physics*, *122*(2), 1439–1450. https://doi.org/10.1002/2016JA023269

Carlson, C., Curtis, D., Paschmann, G., & Michel, W. (1982). An instrument for rapidly measuring plasma distribution functions with high resolution. *Advances in Space Research*, *2*(7), 67–70. https://doi.org/10.1016/0273-1177(82)90151-X

Collinson, G. A., Dorelli, J. C., Avanov, L. A., Lewis, G. R., Moore, T. E., Pollock, C., et al. (2012). The geometric factor of electrostatic plasma analyzers: A case study from the Fast Plasma Investigation for the Magnetospheric Multiscale mission. *Review of Scientific Instruments*, *83*(3), 033303. https://doi.org/10.1063/1.3687021

Dahl, D. A. (2000). Simion for the personal computer in reflection. *International Journal of Mass Spectrometry*, *200*(1), 3–25. https://doi.org/10.1016/S1387-3806(00)00305-5

de Rijk, E., Macor, A., von Bieren, A., Ansermet, J.-P., Maffei, B., Pisano, G., & Hesler, J. (2013). Modular set of corrugated wave-guiding components for applications from 500 to 750 GHz. *2013 38th International Conference on Infrared, Millimeter, and Terahertz Waves (IRMMW-THz)*, 1–2. https://doi.org/10.1109/IRMMW-THz.2013.6665760

Dimitriadis, A., Favre, M., Billod, M., Ansermet, J.-P., & Rijk, E. (2016). Design and fabrication of a lightweight additive-manufactured Ka-band horn antenna array. *2016 10th European Conference on Antennas and Propagation (EuCAP)*, 1–4. https://doi.org/10.1109/EuCAP.2016.7481436

Duvet, L. (2001). *Instrumentation pour l'etude in-situ des atmospheres neutres et ionises planetaires et cometaires: Idm (ion dynamics monitor) et cops (comet pressure sensor)* (p. 34). These de Doctorat.

Fraser, G. (1983). The electron detection efficiency of microchannel plates. *Nuclear Instruments and Methods in Physics Research*, *206*(3), 445–449. https://doi.org/10.1016/0167-5087(83)90381-2

Fraser, G. (2002). The ion detection efficiency of microchannel plates (MCPs). *International Journal of Mass Spectrometry*, *215*(1–3), 13–30. https://doi.org/10.1016/S1387-3806(01)00553-X

Hamamatsu. (2024). Related documents |microchannel plates (MCPs) |Hamamatsu Photonics. Retrieved from https://www.hamamatsu.com/eu/en/product/optical-sensors/electron_ion-sensor/mcp/catalog.html

Heidt, H., Puig-Suari, J., Moore, A., Nakasuka, S., & Twiggs, R. (2000). CubeSat: A new generation of picosatellite for education and industry low-cost space experimentation. In *14th annual/USU conference on small satellites* (p. 1). Utah State University's (USU) Institutional Repository (IR).

Hénaff, G. (2025). Polar-to-energy responses of Sectors A-D for the 3DCAM instrument under a 4 keV electron beam. *Zenodo*. https://doi.org/10.5281/zenodo.15056829

Hénaff, G., & Berthomier, M. (2025). Parametric Study of the performance of an electrostatic analyzer with an hemispheric field-of-view based on the donut topology. *Journal of Geophysical Research: Space Physics*, *130*(3), e2024JA033367. https://doi.org/10.1029/2024JA033367

Hooks, D. E., Carpenter, B., Hickethier, M., Clark, C., Brown, N., McBride, M., et al. (2024). Ultra-black coatings for space instruments: A comparison of traditional Ebonol C processes and a method for future repeatability. *Journal of Manufacturing Processes*, *113*, 230–237. https://doi.org/10.1016/j.jmapro.2024.01.057

Johnstone, A. D., Alsop, C., Burge, S., Carter, P. J., Coates, A. J., Coker, A. J., et al. (1997). Peace: A plasma electron and Current experiment. In C. P. Escoubet, C. T. Russell, & R. Schmidt (Eds.), *The cluster and Phoenix missions* (pp. 351–398). Springer Netherlands. https://doi.org/10.1007/978-94-011-5666-0_13

Larrick, Q., Pollock, C., Hampton, D., Avanov, L., Gershman, D., Thorsen, D., et al. (2024). Additively manufactured plastic plasma spectrometer. *Review of Scientific Instruments*, *95*(11), 114503. https://doi.org/10.1063/5.0219571

Li, J., Guo, C., Mao, L., Xiang, J., Huang, G.-L., & Yuan, T. (2018). Monolithically 3-D printed hemispherical resonator waveguide filters with improved out-of-band rejections. *IEEE Access*, *6*, 57030–57048. https://doi.org/10.1109/ACCESS.2018.2872696

McComas, D., Allegrini, F., Bagenal, F., Casey, P., Delamere, P., Demkee, D., et al. (2008). The Solar Wind Around Pluto (SWAP) instrument aboard new Horizons. *Space Science Reviews*, *140*(1), 261–313. https://doi.org/10.1007/s11214-007-9205-3

McComas, D. J., Alexander, N., Allegrini, F., Bagenal, F., Beebe, C., Clark, G., et al. (2017). The Jovian Auroral Distributions Experiment (JADE) on the Juno Mission to Jupiter. *Space Science Reviews*, *213*(1), 547–643. https://doi.org/10.1007/s11214-013-9990-9

McComas, D. J., Allegrini, F., Pollock, C. J., Funsten, H. O., Ritzau, S., & Gloeckler, G. (2004). Ultrathin (10 nm) carbon foils in space instrumentation. *Review of Scientific Instruments*, *75*(11), 4863–4870. https://doi.org/10.1063/1.1809265

McComas, D. J., Zirnstein, E. J., Bzowski, M., Dayeh, M. A., Funsten, H. O., Fuselier, S. A., et al. (2017). Seven years of imaging the global heliosphere with IBEX. *The Astrophysical Journal - Supplement Series*, *229*(2), 41. https://doi.org/10.3847/1538-4365/aa66d8

McFadden, J. P., Carlson, C. W., Larson, D., Ludlam, M., Abiad, R., Elliott, B., et al. (2008). The THEMIS ESA plasma instrument and In-flight calibration. *Space Science Reviews*, *141*(1–4), 277–302. https://doi.org/10.1007/s11214-008-9440-2

Morel, X., Berthomier, M., & Berthelier, J.-J. (2017). Electrostatic analyzer with a 3-D instantaneous field of view for fast measurements of plasma distribution functions in space. *Journal of Geophysical Research: Space Physics*, *122*(3), 3397–3410. https://doi.org/10.1002/2016JA023596

National Academies of Sciences, E. (2025). *The next decade of discovery in solar and space physics: Exploring and safeguarding humanity: Home in space*. The National Academies Press. https://doi.org/10.17226/27938

Neugebauer, M., & Snyder, C. W. (1962). Solar plasma experiment. *Science (New York, N.Y.)*, *138*(3545), 1095–1097. https://doi.org/10.1126/science.138.3545.1095-a

Orsini, S., Livi, S. A., Lichtenegger, H., Barabash, S., Milillo, A., De Angelis, E., et al. (2021). SERENA: Particle instrument suite for determining the sun-mercury interaction from BepiColombo. *Space Science Reviews*, *217*(1), 11. https://doi.org/10.1007/s11214-020-00787-3

Owen, C. J., Bruno, R., Livi, S., Louarn, P., Janabi, K. A., Allegrini, F., et al. (2020). The Solar Orbiter Solar Wind Analyser (SWA) suite. *Astronomy and Astrophysics*, *642*, A16. https://doi.org/10.1051/0004-6361/201937259

Perera, A. T. K., Song, K., Umezu, S., & Sato, H. (2023). Recent progress in functionalized plastic 3D printing in creation of metallized architectures. *Materials and Design*, *232*, 112044. https://doi.org/10.1016/j.matdes.2023.112044

Pollock, C., Moore, T., Jacques, A., Burch, J., Gliese, U., Saito, Y., et al. (2016). Fast plasma investigation for Magnetospheric Multiscale. *Space Science Reviews*, *199*(1–4), 331–406. https://doi.org/10.1007/s11214-016-0245-4

Rème, H., Aoustin, C., Bosqued, J. M., Dandouras, I., Lavraud, B., Sauvaud, J. A., et al. (2001). First multispacecraft ion measurements in and near the Earth's magnetosphere with the identical Cluster ion spectrometry (CIS) experiment. *Annales Geophysicae*, *19*(10/12), 1303–1354. https://doi.org/10.5194/angeo-19-1303-2001

Rème, H., Bosqued, J. M., Sauvaud, J. A., Cros, A., Dandouras, J., Aoustin, C., et al. (1997). The cluster ion spectrometry (CIS) experiment. *Space Science Reviews*, *79*(1), 303–350. https://doi.org/10.1023/A:1004929816409

Retinò, A., Khotyaintsev, Y., Le Contel, O., Marcucci, M. F., Plaschke, F., Vaivads, A., et al. (2022). Particle energization in space plasmas: Towards a multi-point, multi-scale plasma observatory. *Experimental Astronomy*, *54*(2), 427–471. https://doi.org/10.1007/s10686-021-09797-7

Ritzau, S. M., & Baragiola, R. A. (1998). Electron emission from carbon foils induced by keV ions. *Physical Review B*, *58*(5), 2529–2538. https://doi.org/10.1103/PhysRevB.58.2529

Saito, Y., Delcourt, D., Hirahara, M., Barabash, S., André, N., Takashima, T., et al., BepiColombo Mio/MPPE Team. (2021). Pre-flight calibration and near-earth commissioning results of the Mercury Plasma Particle Experiment (MPPE) onboard MMO (Mio). *Space Science Reviews*, *217*(5), 70. https://doi.org/10.1007/s11214-021-00839-2

Saito, Y., Yokota, S., Asamura, K., Tanaka, T., Nishino, M. N., Yamamoto, T., et al. (2010). In-flight performance and initial results of plasma energy angle and composition experiment (PACE) on SELENE (Kaguya). *Space Science Reviews*, *154*(1), 265–303. https://doi.org/10.1007/s11214-010-9647-x

Sauvaud, J.-A., Larson, D., Aoustin, C., Curtis, D., Médale, J.-L., Fedorov, A., et al. (2008). The IMPACT Solar Wind Electron Analyzer (SWEA). *Space Science Reviews*, *136*(1–4), 227–239. https://doi.org/10.1007/s11214-007-9174-6

Scudder, J., Hunsacker, F., Miller, G., Lobell, J., Zawistowski, T., Ogilvie, K., et al. (1995). Hydra—A 3-dimensional electron and ion hot plasma instrument for the POLAR spacecraft of the GGS mission. *Space Science Reviews*, *71*(1), 459–495. https://doi.org/10.1007/BF00751338

Teniente, J., Iriarte, J. C., Caballero, R., Valcázar, D., Goñi, M., & Martínez, A. (2018). 3-D printed horn antennas and components performance for space and telecommunications. *IEEE Antennas and Wireless Propagation Letters*, *17*(11), 2070–2074. https://doi.org/10.1109/LAWP.2018.2870098

Vaisberg, O., Berthellier, J.-J., Moore, T., Avanov, L., Leblanc, F., Leblanc, F., et al. (2016). The 2π charged particles analyzer: All-sky camera concept and development for space missions. *Journal of Geophysical Research: Space Physics*, *121*(12), 11750–11765. https://doi.org/10.1002/2016JA022568

von Bieren, A., de Rijk, E., Ansermet, J.-P., & Macor, A. (2014). Monolithic metal-coated plastic components for mm-wave applications. In *International conference on infrared, Millimeter, and Terahertz waves, IRMMW-THz*. https://doi.org/10.1109/IRMMW-THz.2014.6956222

Yokota, S., Saito, Y., & Asamura, K. (2024). A low-energy particle experiment for both ion and electron measurements using a single microchannel plate-based detector. *Earth Planets and Space*, *76*(1), 50. https://doi.org/10.1186/s40623-024-01997-7

Yokota, S., Saito, Y., Asamura, K., & Mukai, T. (2004). Development of an ion energy mass spectrometer for application on board three-axis stabilized spacecraft. *Review of Scientific Instruments*, *76*(1), 014501. https://doi.org/10.1063/1.1834697

Young, D. T., Berthelier, J. J., Blanc, M., Burch, J. L., Coates, A. J., Goldstein, R., et al. (2004). Cassini plasma spectrometer investigation. *Space Science Reviews*, *114*(1), 1–112. https://doi.org/10.1007/s11214-004-1406-4

Ziegler, J. F., Ziegler, M., & Biersack, J. (2010). SRIM – The stopping and range of ions in matter (2010). *Nuclear Instruments and Methods in Physics Research Section B: Beam Interactions with Materials and Atoms*, *268*(11–12), 1818–1823. https://doi.org/10.1016/j.nimb.2010.02.091

Zurbuchen, T. H., & Gershman, D. J. (2016). Innovations in plasma sensors. *Journal of Geophysical Research: Space Physics*, *121*(4), 2891–2901. https://doi.org/10.1002/2016JA022493